Removing Instability-Caused Low-Frequency Features in Small Perturbation Spectra of Perovskite Solar Cells

Sandheep Ravishankar[1,2], Marisé Garcia-Batlle[2], Juan Bisquert[2], Germá Garcia-Belmonte[2,*], Jann Odrobina[3], Carl-Albrecht Schiller[3]

[1]IEK-5 Photovoltaics, Forschungszentrum Jülich, 52425 Jülich, Germany

[2]Institute of Advanced Materials (INAM), Universitat Jaume I, 12006 Castelló, Spain

[3]Zahner-elektrik GmbH & Co KG, 96317 Kronach, Germany

**Email: garciag@uji.es*

Abstract

Small-perturbation frequency-domain techniques such as impedance spectroscopy (IS) and intensity-modulated photocurrent spectroscopy (IMPS) have become important methods for the investigation of the physical working mechanisms of the perovskite solar cell (PSC). The validity of these methods relies on assuming sample stability at the given steady state. Through a series of IMPS measurements, we identify that this assumption is invalid in certain cases for both iodide and bromide-based PSCs that show strong time drift in their IMPS response, noticeable in particular at low frequencies, which are usually connected with the kinetics of ionic motion and interaction with outer electrodes. Using time course interpolation and a corrective Z-HIT algorithm that connects the modulus of the IMPS transfer function and its phase, we identify that the low-frequency arc/tail is in certain cases an artefact generated by time drift of the sample. Since the low-frequency data in an IMPS measurement of the PSC provide important information regarding its differential external quantum efficiency, care must be taken to ascertain the origin and validity of the low-frequency phenomena. Validity test is performed by using a combination of corrective algorithms mentioned above and several measurements over time to obtain stabilized spectra virtually free of time drift.

1. Introduction

Perovskite solar cells (PSCs) have reached very high efficiencies, both in a single junction (25.2%) and tandem configuration (29.2%),[1] confirming its potential to prove a disruptive technology for the renewable energy scene in the near future. This rapid development is related to a large amount of information obtained regarding the physical operation mechanisms of the PSC.[2] A very popular method to obtain such information in solar cells in general and PSCs in particular, is the use of small perturbation frequency domain methods. While impedance spectroscopy (IS) has been the most widely used and well-known small perturbation measurement for solar cells,[3-4] intensity modulated photocurrent spectroscopy (IMPS) has emerged as an alternative technique that provides both novel and complementary information regarding the working mechanisms of the PSC.[5-8]

A basic assumption during an IMPS measurement, and in general all small perturbation measurements, is the stability of the system under scrutiny. Any change or drift in the steady-state condition of the system during the measurement, due to degradation or other effects, can significantly affect the output, especially at low frequencies that require longer measurement times[9]. Other factors to be considered also include the linearity in the response to the applied perturbation and the condition of causality, which stipulates a response only after application of the stimulus. The latter condition gives rise to the Kramers-Kronig (KK) relations[10-11] that relate the real part of the complex transfer function to its imaginary part and vice versa. The KK relations provide a well-known methodology to verify the response of small perturbation measurements.[12]

From previous analyses, it is well established that the low frequency capacitance (<10 Hz) at 300 K, reaches values exceeding 10 μF cm^{-2}, practically independent of the perovskite absorber film thickness.[13] This dark capacitance cannot be associated with bulk dielectric relaxation and relates to ionic accumulation in the vicinity of the outer electrodes. Kinetics of ion accumulation reproduces in some cases diffusion patterns. Moreover, low-frequency features are connected to the appearance of hysteresis in the current density–voltage curves.[2] In brief, previous analyses[14-16] led to the idea that the large low-frequency capacitance relates to the interactions of ions to the interface by a complex mechanism that might involve not only ion diffusion and accumulation, but also electrode reactivity and ionic-electronic coupling. Hence, it would be particularly interesting to verify if the low-frequency features usually observed in PSC using IS and IMPS appear as an effect of time instabilities and response drift or, on the contrary, derive from stable physical mechanisms.

In this work, we establish the role of time drift as a source of error in IMPS measurements carried out on methylammonium lead iodide and methylammonium lead bromide PSCs. It is well known that the PSC exhibits very slow response timescales on the order of seconds, related to the slow drift of ions within its lattice.[2, 17-18] This behaviour creates a large sensitivity to experimental parameters of voltage and light intensity that makes it difficult to maintain a given steady state in the case of small perturbation techniques. We confirm the occurrence of drift in the system state through a time-dependent series of IMPS measurements that leads to variations in the obtained IMPS spectra. By applying corrective time course interpolation and the method of Z-

HIT refinement, we identify that the low frequency (LF) IMPS response, which is an arc/tail in the lower or upper quadrant, is in certain cases only an artefact produced by the time drift of the sample. The validity of the data, especially at low frequencies, is very important due to the fact that the IMPS transfer function contains information on the external quantum efficiency of the solar cell. Therefore, careful accounting and subsequent application of the corrective procedures will prove important in error-free characterisation of high-efficiency PSCs using small perturbation frequency domain methods.

2. Methods

2.1 Sample preparation

All materials were used in our experiments as received: FTO glasses (25 x 25 mm, Pilkington TEC 15, ~ 15 Ω sq^{-1} resistance), TiO_2 paste (Dyesol 30 NRD, 300 nm average particle size), CH_3NH_3Br, CH_3NH_3I (DYESOL), $PbBr_2$, PbI_2 (TCI, 99.99%), titanium diisopropoxide (bis-acetylacetonate) (75% in isopropanol, Sigma-Aldrich), N,N-dimethylformamide anhydrous (Sigma Aldrich, 99.8%), dimethylsulfoxide anhydrous (Sigma Aldrich, ≥ 99.9 %), toluene anhydrous (Sigma Aldrich, 99.8 %) and chlorobenzene anhydrous (Sigma Aldrich, 99.8 %) and spiro-OMeTAD (Merck).

Preparation of photoanode. Prior to the deposition of TiO_2 compact layer, the FTO substrate was partially etched with zinc powder and HCl (2 M) and cleaned by ultra-sonication in Hellmanex detergent diluted at 2%, rinsed with Milli-Q water and in a solution of ethanol: isopropanol (1:1 v/v). After that, the substrates were treated in a UV−O_3 cleaner for 10 min.

Compact layer TiO_2. The TiO_2 blocking layer was deposited by aerosol spray pyrolysis at 450 °C, using a commercial titanium diisopropoxide bis(acetylacetonate) solution (75% in 2-propanol, Sigma-Aldrich) diluted in ethanol (1:9, v/v) as precursor, with oxygen as carrier gas and spraying a total volume of 10 mL (approx.), performed by 3 steps spraying of 6 s each one and waiting 30 s between steps.

*Mesoporous layer TiO_2.*To form the mesoporous layer, diluted paste of TiO_2 (1:5, weight ratio) (Dyesol 30NRD: ethanol) was spin-coated at 2000 rpm for 10 s followed by 100ºC for 10 min and sintering step at 500ºC for 30 min under room atmosphere.

Deposition of perovskite. For cells 1, 2, 3, and 4 the perovskite precursor solution was prepared by mixing N,N-dimethylformamide (DMF) solutions containing MAI and PbI_2 (1: 1 mol %) and MAI, PbI_2 and dimethylsulphoxide (DMSO 1: 1: 1 mol %). Then, 50 µL of perovskite precursor was spin-coated at 4000 rpm for 50 s. Chlorobenzene anhydrous was used as the anti-solvent was added just before the white solid begins to crystallize in the substrate. In the case of bromine cell, $MAPbBr_3$ film was prepared by mixing $PbBr_2$ precursor solution in DMF and DMSO without stirring at 80°C for 20 minutes until complete dissolve. After cool down at room temperature, this solution was mixed with MABr powder to obtain a final concentration of 1.4 M $MAPbBr_3$. The solution was deposited by two ramps of spin coating method: 1000 rpm for 10 s and 4000 rpm for 40s, using toluene as anti-solvent during the second ramp. This was followed by annealing at 100°C for 3 min to obtain a shiny and homogenous film.

Deposition of hole transporting material (HTM) and device fabrication. To complete the fabrication of device, a solution of Spiro-OMeTAD as HTM, was prepared by dissolving 72.3 mg of (2,2′,7,7′-tetrakis(N,N′-di-pmethoxyphenylamine)- 9,9′-

spirobifluorene) in 1 mL of chlorobenzene, 28.8 μL of 4-tert-butylpyridine and 17.5 μL of a stock solution of 520 mg/mL of lithium bis- (trifluoromethylsulfonyl) imide in acetonitrile, as additives. Perovskite film was then covered with 50 μL of the HTM solution by dynamically spin coating at 4000 rpm, 800 rpm/s of acceleration for 30 s. Finally, 85 nm of gold was thermally evaporated on top of the device as a back contact, using a commercial Univex 250 chamber, from Oerlikon Leybold Vacuum.

2.2 IMPS Theory

The IMPS transfer function is defined as[8]

$$Q(\omega) = \frac{\widetilde{J_e}}{\widetilde{J_\Phi}} \tag{1}$$

where the tilde represents an AC quantity, j_e is the extracted current density (A/cm^2) and $j_\phi = q\phi$ is the input photon flux ϕ represented as a current density. Note that the definition in Equation 1 is dimensionless. Its LF limit is

$$Q(0) = \frac{d\overline{J_e}}{d\overline{J_\Phi}} \tag{2}$$

where the overbar represents a steady-state value. Therefore, the LF limit of the IMPS transfer function yields the differential external quantum efficiency $EQE_{PV-diff}$ and the real part of the IMPS transfer function Q' yields the frequency-dependent evolution of $EQE_{PV-diff}$.The absolute or steady-state external quantum efficiency is given by

$$EQE_{PV-SS} = \frac{\overline{J_e}}{\overline{J_\Phi}} \tag{3}$$

From Equations 2 and 3, we can see that the $EQE_{PV-diff}$ is the slope of the DC photocurrent versus light intensity.

Alternatively, the IMPS spectra can be calculated by converting the output specific responsivity values j (A/W·m^2) into the Q form by using

$$Q(\omega) = \tilde{j}(\omega)\frac{hc}{q\lambda A} \tag{4}$$

where h is Planck's constant, c is the speed of light, q is the electronic charge, $\lambda = 454$ nm is the wavelength of the input photons and $A = 10^{-5}$m^2 is the illuminated area on the solar cell.

2.3 IMPS measurements

A Zahner CIMPS[19] system (Figure 1) was used to carry out the IMPS measurements. Such a setup is advantageous compared to the traditional instrumentation. CIMPS stands for "Controlled Intensity Modulated Photo Spectroscopy", what signals, that the set point magnitude, respectively reference magnitude controlled by the FRA output as well as the FRA reference input is not the LED current like usual. Instead, it is the directly controlled intensity as set signal and the immediately measured intensity as FRA reference input signal. This is realized by means of a photo sensor close to the site of the sample. The sensor receives a fixed calibrated share of the intensity at cell site. The output is also used as feedback signal for an extra power operational amplifier (*PP211*) controlling the LED light source. This feedback loop eliminates any non-linearity, thermal and time degradation of the light source in a way that a factory calibration once is sufficient to guarantee calibrated results for both intensity bias as well as modulation within the lifetime of the LED. Because the (immediately measured) intensity is used as FRA reference input signal instead of the LED current (as a substitute quantity),

modulus magnitude error as well as phase shift between intensity and cell output signal (current for IMPS, voltage for IMVS) is eliminated.

Most measurements were carried out at potentiostatic condition with zero set voltage (short circuit condition) in the frequency range 10^5 Hz–0.1 Hz, except of the measurement series displayed in Figure 6c and d, which was acquired down to 10^{-2} Hz. A blue LED light source emitting at wavelength 454 nm with a spectral half width of 12 nm was used for all the measurements under DC bias of 500 W/m^2 with an AC amplitude of 10% of the DC light intensity used.

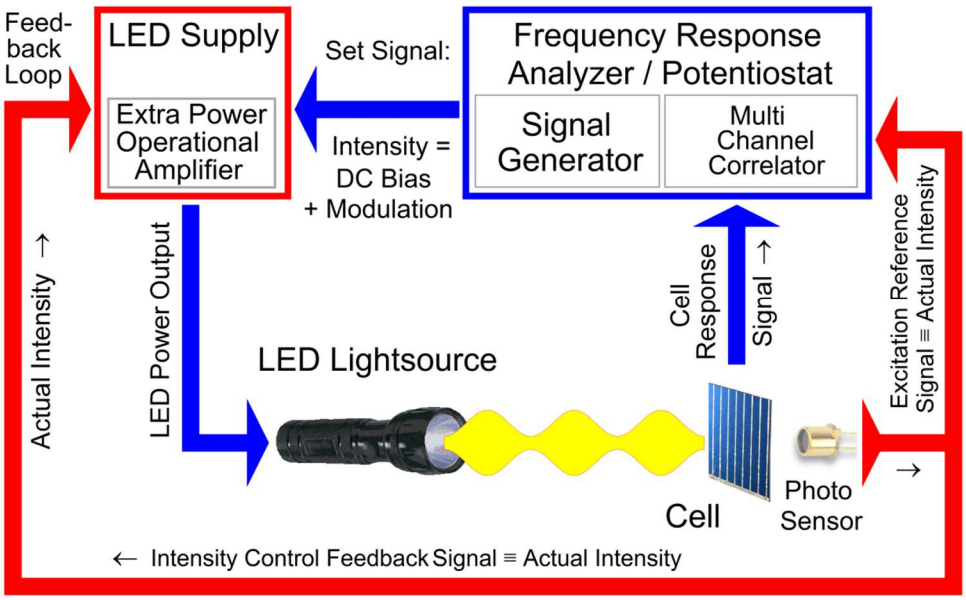

Figure 1 Functional scheme of the CIMPS setup used during IMPS measurements. The cell is kept under potentiostatic control by the FRA/potentiostat (*Zennium Pro*). For IMVS measurements, the potentiostat can be switched to galvanostatic mode or off. Components and signal paths different from the classical IMPS setup are marked in red.

2.4 Equivalent circuit model

The equivalent circuit (EC) recently developed[7] to analyze IMPS data of PSC is shown in Figure 2a. This model expands the traditional equivalent circuit of IS[3-4] and produces three spectral features: two arcs in the upper quadrant and one in the lower quadrant as its IMPS response, see Figure 2b. While the same EC produces the IS spectrum shown in Figure 2c.

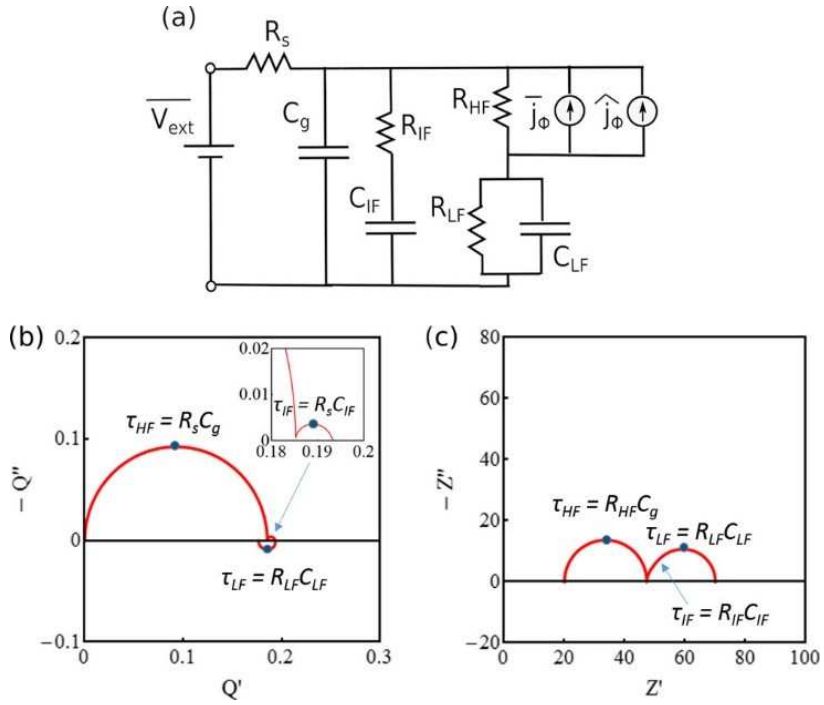

Figure 2 (a) Equivalent circuit of the PSC during an IMPS measurement, identified in Ref.[7]. (b) IMPS and (c) IS spectra. The elements include a series resistance R_s, external DC voltage $\overline{V_{ext}}$, geometric capacitance C_g, DC current source $\overline{j_\phi}$ and modulated current source $\widehat{j_\phi}$ representing photogeneration, resistances R_{HF}, R_{IF} and R_{LF} corresponding to high, intermediate and low frequency respectively, capacitances C_{IF} and C_{LF} corresponding to intermediate and low frequency respectively. The characteristic times constants are indicated in the complex plane plots of the spectra.

The high frequency (HF) arc in the upper quadrant is formed by the series resistance R_s and geometric capacitance C_g. The intermediate frequency (IF) line is optional, depending on the observation of an IF arc or not in the upper quadrant. The LF arc is formed by the time constant of the LF capacitance and resistance. This arc shifts to the lower quadrant due to the placement of the current source that represents the modulated light source in an IMPS measurement across only the HF resistance. Furthermore, the LF limit of the IMPS transfer function, which is the horizontal axis intercept of the LF arc/tail, provides information on the $EQE_{PV-DIFF}$ of the solar cell.

2.5 Z-HIT algorithm for KK transformation

The use of the KK relations in practical applications yields several limitations that create error, such as the need for extrapolation of measured data due to the integration frequency range (−∞, +∞) and the inability to detect all-pass contributions.[20] From the logarithmic counterpart of the linear KK relations, often addressed as Hilbert transform, an advantageous alternative procedure was derived which takes the two-pole nature of the system into account. It uses an approximate relation between the logarithm of the modulus of the small-perturbation complex transfer function Q (see below for the specific case of IMPS) and its phase shift versus the logarithm of the frequency. This procedure is able to overcome the above mentioned limitations and is written as[21]

$$\ln|Q(\omega_0)| \approx const. + \frac{2}{\pi}\int_{\omega_s}^{\omega_0} \varphi(\omega) d\ln\omega + \gamma \frac{d\varphi(\omega_0)}{d\ln\omega} \quad (5)$$

where ω_s and ω_0 are the starting frequency of the integration and the frequency of interest respectively, φ is the phase angle of the complex function and γ is a constant with a value of $-\pi/6$ independent of the nature of the system.[20] This relation is used in a commercially available software package, termed the Z-HIT algorithm, in order to check the validity of the experimental data and detect unwanted time drift contaminations. Due to the relative robustness of the phase angle φ compared to the vulnerability of the small-perturbation transfer function modulus by time drift effects, the Z-HIT algorithm can also be used to reconstruct the course of the uncontaminated $Q(\omega)$ from the phase course $\varphi(\omega)$ of the experimental data.

2.6 Time course interpolation

It is possible to carry out time course interpolation to account for time drift of the small perturbation spectra, especially at lower frequencies, see Figure 3. This procedure was presented by H. Göhr and W. Meißner[22-23] the late 1970s and is since then content of the commercial Thales software. A better known similar approach was published by Savova-Stoynov and Stoynov,[24-25] whose procedure is summarised in Ref.[20].

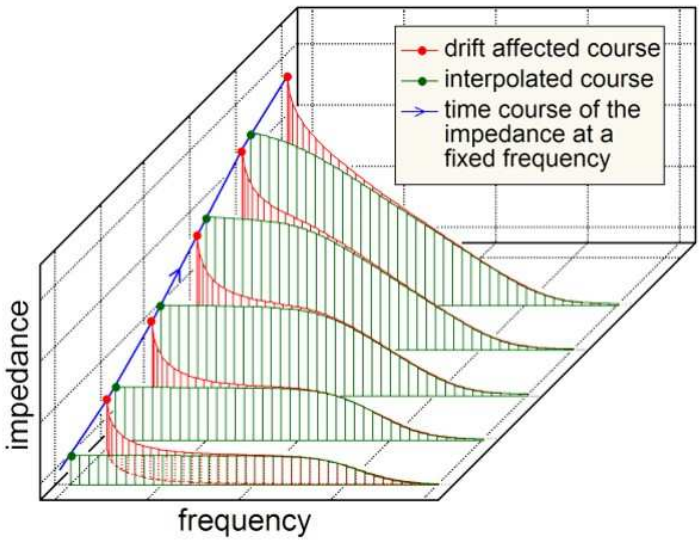

Figure 3 Scheme of the time course interpolation operation here illustrated for the case of impedance (Bode diagram). Series of measured spectra beginning at high frequencies (right) are displayed in red, with their samples also moving in the time direction along the z-axis ("bent" in time) as measurement time evolves at low frequencies. Along the time course at every certain frequency through the series (blue curve), the individual samples (green lines) of the impedance at a certain fixed time (here the spectrum start time) are reconstructed by interpolation. The procedure can be performed analogously with IMPS and IMVS data.

3. Results and discussion

The structure and expected band alignment[26] of the cells used for this study and their corresponding current density–voltage (*j-V*) curves are shown in Figures 4a and 4b, respectively. A total of five cells were measured, with four of them corresponding to the methylammonium lead iodide ($CH_3NH_3PbI_3$) perovskite absorber and one cell corresponding to methylammonium lead bromide ($CH_3NH_3PbBr_3$) absorber, as explained in the Methods section. These cells are hereafter referred to as cells I1-I4 and B1 respectively. As can be seen in Figure 4c, the I1-I4 cells showed differences mainly in their short-circuit current (j_{sc}), ranging between 15-20 mA/cm^2, while their open-circuit voltages were very similar, between 1.00–1.05 V. The observed dispersion in short-circuit current is connected to the particularities of the preparation and processing conditions. It is well known that the quality of the perovskite film formed on the substrate is an important factor that controls the output j_{sc}, influenced by a good connection to the back contact, sufficient mobility and good contact between grains. We therefore ascribe the variations in the j_{sc} values of the cells I1-I4 to the limited reproducibility, inherent error and imperfections formed in the spin-coating process of these films.[27]

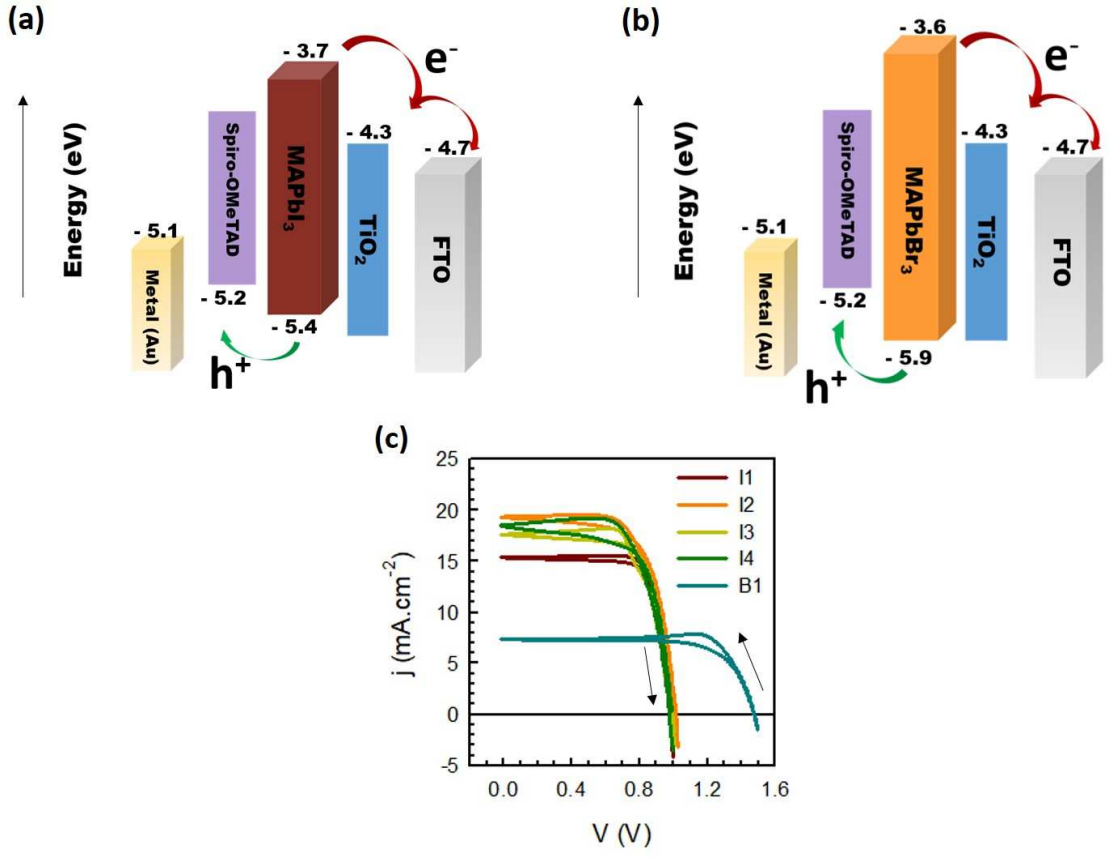

Figure 4 Schematic of the structure and energy levels of the measured (a) Iodide PSCs and (b) Bromide PSC. (c) Corresponding *j-V* curves of the PSCs used for IMPS measurements, measured at a scan rate of 50 mV/s. The arrows indicate the direction of scan. The measurements were carried out using a blue LED emitting at 454 nm with an

intensity of 500 W/m^2, that corresponds to a photon flux of 1.1×10^{17} cm^{-2} s^{-1} (AM 1.5G illumination corresponds to a photon flux of 4.3×10^{17} cm^{-2} s^{-1}).

We proceeded to measure the IMPS spectra of the cells at short-circuit (SC) conditions followed by time course interpolation and Z-HIT correction to the obtained spectra (see Methods section). The normalized IMPS spectra (real part versus imaginary part of the dynamic Q transfer function) measured at SC conditions for the cells I1 and I2 are shown in the red lines of Figures 5a and 5b. The spectra were registered soon after the corresponding *j*-*V* curves.

As explained in the Methods section, the low frequency value the real part of the IMPS transfer function Q' yields the frequency-dependent evolution of the differential external quantum efficiency $EQE_{PV-diff}$.[5, 8] In turn, $EQE_{PV-diff}$ relates to the absolute or steady-state external quantum efficiency EQE_{PV-SS}, depending on the linearity in response of the steady-state photocurrent to the input light intensity.[8] The significance of the low-frequency (LF) arc/tail for understanding the operation of the PSC is related to the equivalent circuit (EC) shown in the Methods section (Figure 2). The complex plane diagrams in Figure 5 exhibit two arcs in the upper quadrant, moving towards increasing values of $EQE_{PV-diff}$. We observe that at low frequencies the second arc tails off into a reduction in the Q' values. In this case, while the LF reduction in the $EQE_{PV-diff}$ occurs, the data remains in the upper quadrant.

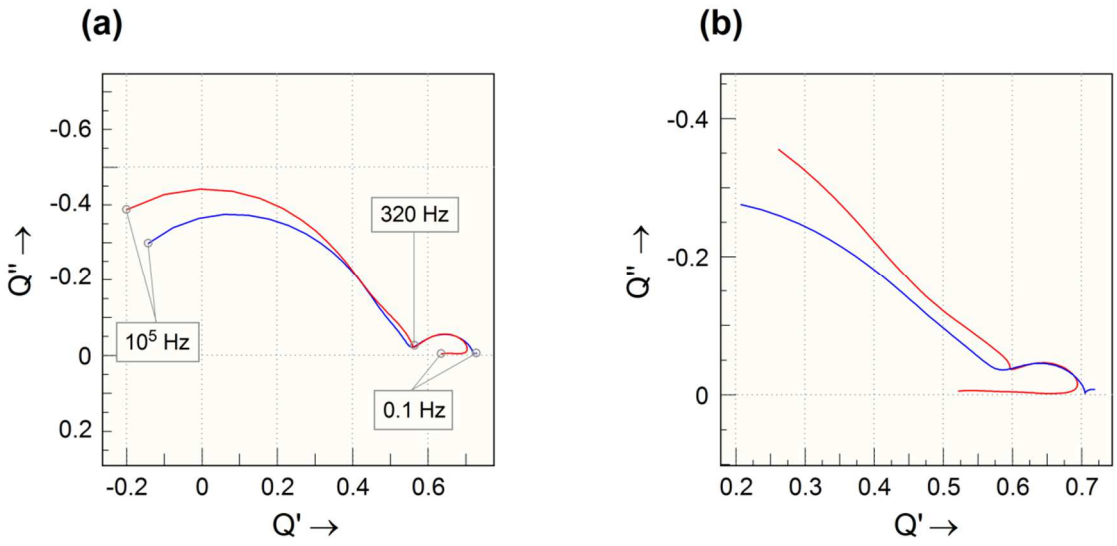

Figure 5 Complex plane diagram of the normalized IMPS transfer function Q for (a) cell I1 (b) cell I2. The red lines correspond to the measured data and the blue lines correspond to the Z-HIT corrected data (see Methods section).

Due to the physical significance of the LF arc on *EQE* assessment, ascertaining the validity of this spectral feature through time course interpolation and Z-HIT correction that accounts for artefacts generated by time drift (see Methods section) is extremely important. Moreover, LF features directly impact the EC and hence the understanding of the physical mechanisms governing the PSC operation.

The Z-HIT corrected spectra are shown in the same graphs of Figures 5a and 5b (blue

lines). It can be seen that for both the cells in the high-frequency (HF) region, there is some variation in the spectra, while the intermediate-region (IF) spectra match quite well. The major discrepancy occurs in the LF region, where the reduction in the real part (around 10% of maximum real value) is not observed for the corrected spectra. These results indicated that time drift in the spectra, especially at lower frequencies, was a significant error factor in our measurements.

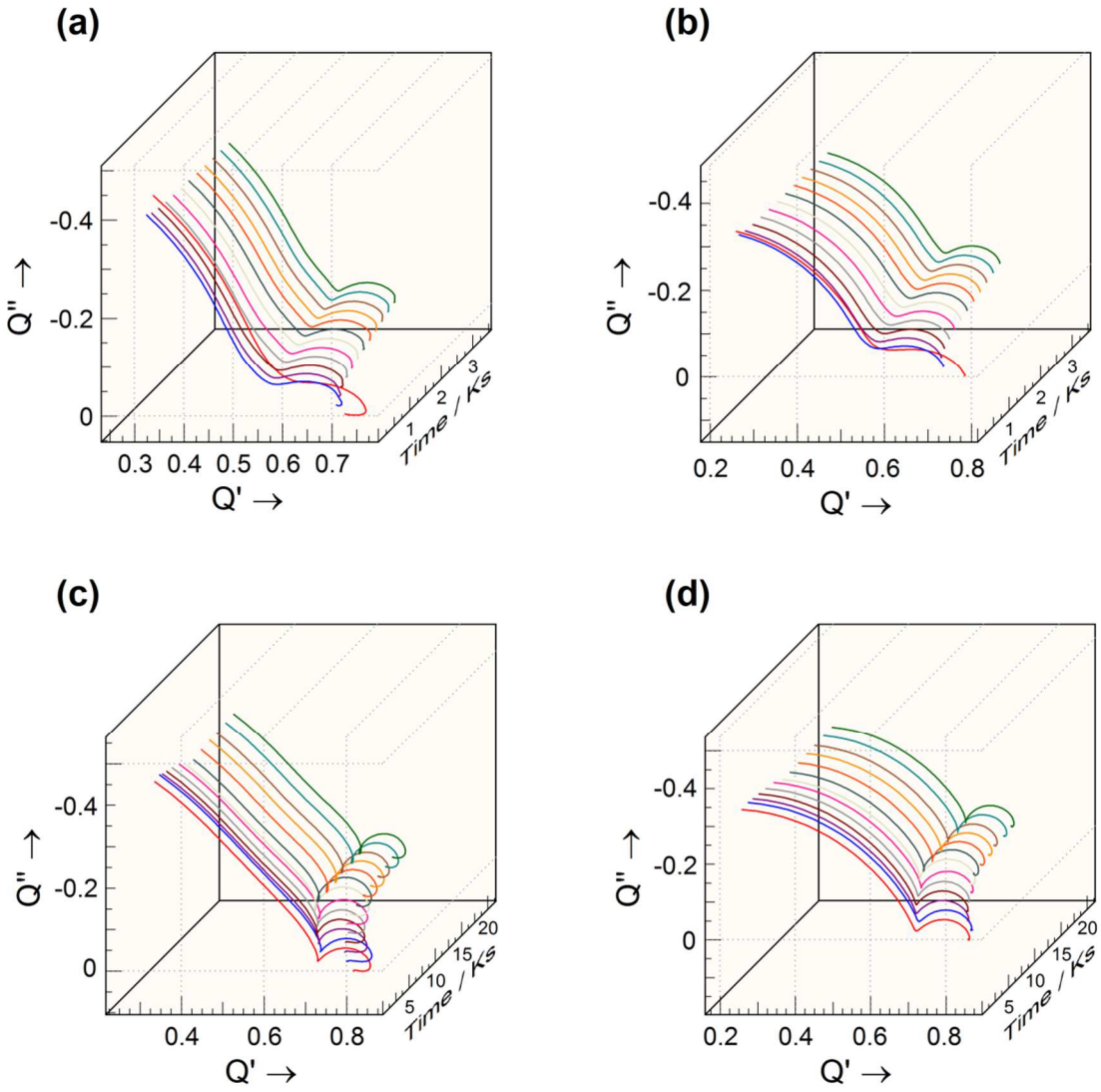

Figure 6 (a, c) Raw data of IMPS series measurements over time of cells I3 and I4 respectively and (b, d) time course interpolation + Z-HIT corrected data (see Methods section) of cells I3 and I4 respectively.

In order to gain deeper insight on the LF effect, we proceeded to carry out a series of IMPS measurements over time on cells I3 and I4, shown in Figures 6a and 6c respectively. It was observed that there occurs a gradual stabilization of the spectra over timescales > 30 minutes. The initial spectra (comparable those shown in Figure 5) in particular suffer strongly from this time drift phenomenon, showing a large variation in the IF and LF regions compared to the stabilized spectra, while a final exact settling into

steady-state behaviour does not happen even after several hours.

Furthermore, time course interpolation followed by Z-HIT correction (see Methods section and also[28] for a detailed description) was carried out, shown in Figures 6b and 6d for cells I3 and I4 respectively. Generally, the reconstructed spectra differ significantly from the raw data. Firstly, it stands out that the abnormal linear shape of the HF semicircles visible in the raw data of Figures 6a and 6c is changed into normal semicircles after the correction procedure, apparent in Figures 6b and 6d. As can be seen from Figures 6a and 6c, the appearance of an IF arc in addition to the HF arc is common to both samples, while the LF arc in the positive imaginary direction (lower quadrant) visible at first glance in the raw data of cell I3 (Figure 6a) vanishes in the corrected data. In contrast, cell I4 now exhibits an additional small LF loop. Zoomed versions of selected corrected spectra are shown in Figure 7 for a better appreciation of this LF loop. It should be noted that the cell I4 measurement ran down to 10^{-2} Hz, while the cell I3 measurement ended at 0.1 Hz.

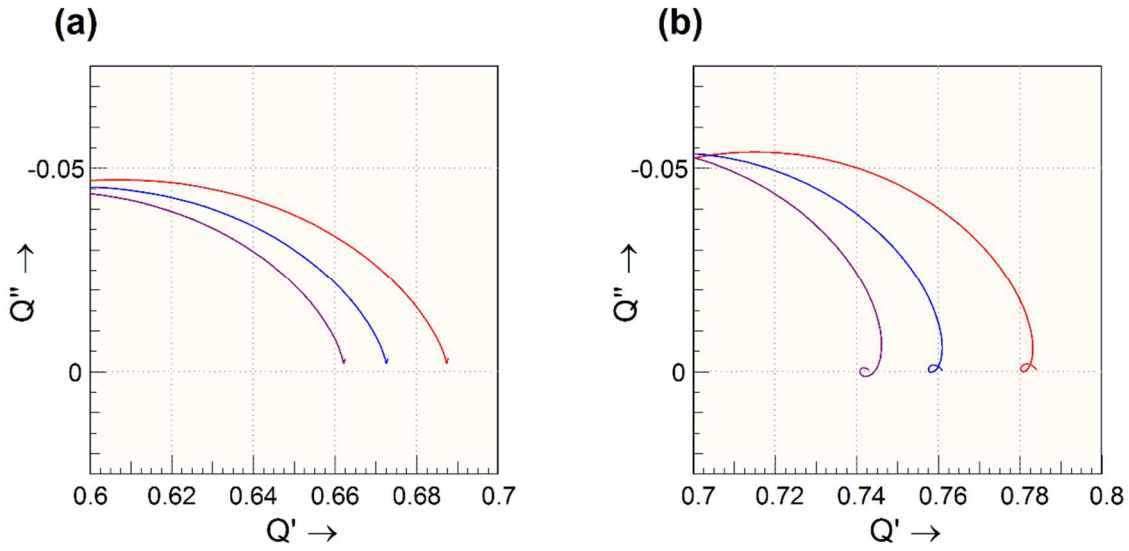

Figure 7 Zoomed complex plane diagram of the IMPS transfer function Q of three selected successive Z-HIT corrected spectra (#3-5) of the IMPS series vs. time for (a) cell I3 and (b) cell I4. It should be noted that the cell I4 measurement ran down to 10^{-2} Hz, while the cell I3 measurement ended at 0.1 Hz.

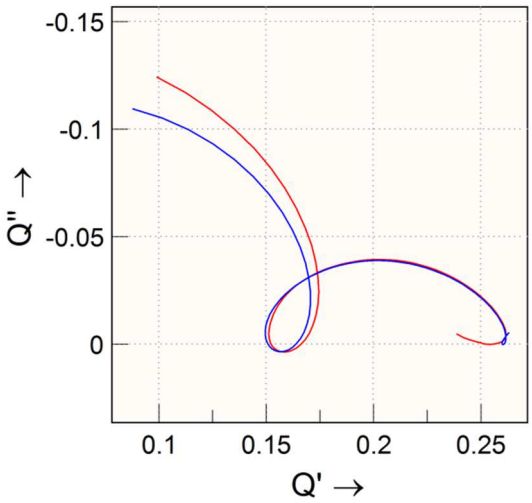

Figure 8 Comparison between raw (red) and Z-HIT-processed IMPS data (blue) of cell B1. Here, the "LF loop" almost vanishes if time drift effect is suppressed while a small loop in the inverse direction comes up at the LF end. The loop in the IF range is obviously real.

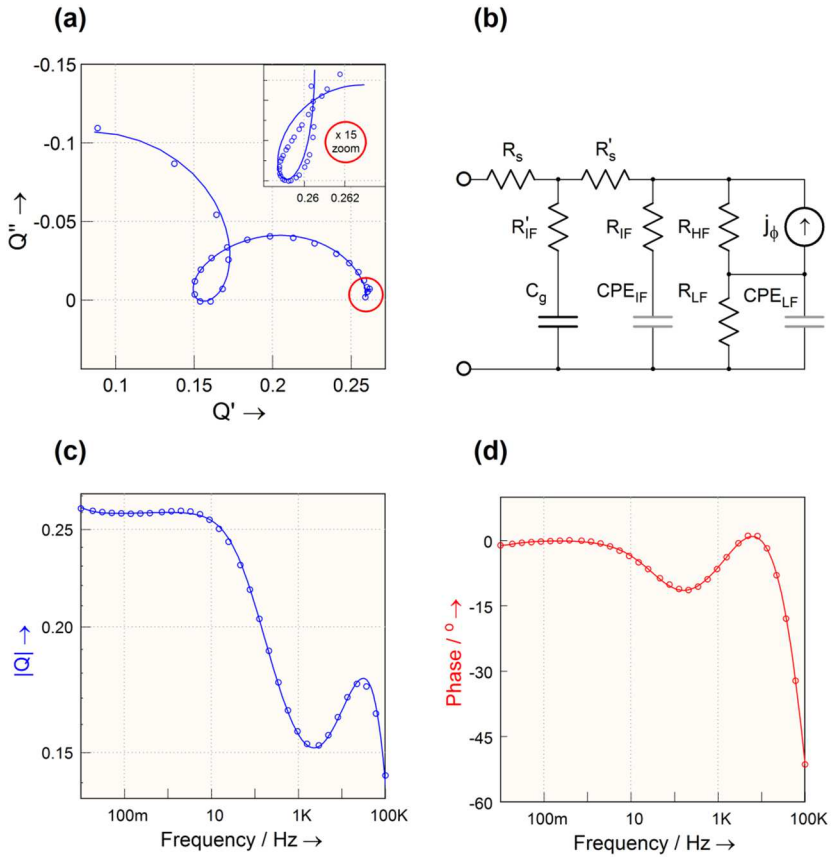

Figure 9 (a) CNLS Fit (Zahner Thales software) of the Z-HIT-processed IMPS data of cell B1. Solid curve: fit; circle symbols: Z-HIT-processed measure data. The number of data points in the LF area of the not zoomed graph is reduced for clearer visibility. (b) A

slightly modified model compared to the EC shown in Figure 2 was used. The Bode diagram modulus (c) and phase (d) confirms the high quality of the fit.

Since the contribution of the LF loop to the net variation of the transfer function is very small, it is tempting to consider that it is only an artefact of the correction procedure. However, a similar feature was also observed in the IMPS spectrum measured for the bromine-based sample (cell B1) shown in Figure 8. It exhibits a similar loop in the LF region but also one in the IF range, very clearly expressed both in the raw as well as processed data. By an extension of the EC in Figure 2, indicated in Figure 9b, we were able to fit the spectrum of cell B1 in Figure 8, shown in Figure 9a (complex plot) and Figure 9c and d (Bode plots). In this case, additional circuit elements are included to properly fit the HF and IF regions of the spectrum. R'_S and R'_{IF} give rise to the intermediate loop (inset of Figure 9a) which is not reproduced with the simpler EC of Figure 2.

This analysis indicates that the loops observed in the LF region are not artefacts of the correction procedure but real phenomena, further indicating the general complexity in the response of the PSC. We remark that the appearance of loops in the IMPS spectra does not require inductive elements in the EC, in contrast to the case of IS.[29] It should also be noted that even the LF loop (zoomed inset in Figure 9a) is reproduced clearly in spite of its small overall contribution and the approximate character of the Z-HIT analysis. In summary, the repetition of spectra and correction of the time drift effect appears an important tool to reveal significant characteristics of small perturbation measurements of PSC, especially at low frequencies.

4. Conclusions

In this work, we have identified that the perovskite solar cell suffers from a drift from its apparent steady-state condition during an IMPS measurement. This can lead to the measurement of erroneous spectra, especially at low frequencies, which are routinely used to extract important information regarding the operation of a solar cell such as its differential external quantum efficiency. By using a corrective algorithm based on time course interpolation and the Z-HIT transformation, we observe that the singular reduction in the differential external quantum efficiency due to the low-frequency arc is eliminated completely in some cases, allowing for a more accurate assessment of the charge extraction properties of the perovskite solar cell using IMPS. In the absence of these corrective measures, it is recommended to carry out a series of IMPS measurements over time in order to obtain stabilized spectra, which we observe to be for timescales greater than 30 minutes.

Acknowledgements

S.R. acknowledges funding from the Helmholtz association via the PEROSEED project. M. G.-B. acknowledges Generalitat Valenciana for grant GRISOLIAP/2018/073.

References

1. National Renewable Energy Laboratory, Best Research-Cell Efficiency Chart. https://www.nrel.gov/pv/cell-efficiency.html (accessed June 1, 2020).

2. Wang, H.; Guerrero, A.; Bou, A.; Al-Mayouf, A. M.; Bisquert, J., Kinetic and Material Properties of Interfaces Governing Slow Response and Long Timescale Phenomena in Perovskite Solar Cells. *Energy Environ. Sci.* **2019**, *12*, 2054-2079.

3. Zarazua, I.; Han, G.; Boix, P. P.; Mhaisalkar, S.; Fabregat-Santiago, F.; Mora-Seró, I.; Bisquert, J.; Garcia-Belmonte, G., Surface Recombination and Collection Efficiency in Perovskite Solar Cells from Impedance Analysis. *J. Phys. Chem. Lett.* **2016**, *7*, 5105-5113.

4. Guerrero, A.; Garcia-Belmonte, G.; Mora-Sero, I.; Bisquert, J.; Kang, Y. S.; Jacobsson, T. J.; Correa-Baena, J.-P.; Hagfeldt, A., Properties of Contact and Bulk Impedances in Hybrid Lead Halide Perovskite Solar Cells Including Inductive Loop Elements. *J. Phys. Chem. C* **2016**, *120*, 8023-8032.

5. Pockett, A.; Eperon, G. E.; Peltola, T.; Snaith, H. J.; Walker, A.; Peter, L. M.; Cameron, P. J., Characterization of Planar Lead Halide Perovskite Solar Cells by Impedance Spectroscopy, Open-Circuit Photovoltage Decay, and Intensity-Modulated Photovoltage/Photocurrent Spectroscopy. *J. Phys. Chem. C* **2015**, *119*, 3456-3465.

6. Ravishankar, S.; Riquelme, A.; Sarkar, S. K.; Garcia-Batlle, M.; Garcia-Belmonte, G.; Bisquert, J., Intensity-Modulated Photocurrent Spectroscopy and Its Application to Perovskite Solar Cells. *J. Phys. Chem. C* **2019**, *123*, 24995-25014.

7. Ravishankar, S.; Aranda, C.; Sanchez, S.; Bisquert, J.; Saliba, M.; Garcia-Belmonte, G., Perovskite Solar Cell Modeling Using Light- and Voltage-Modulated Techniques. *J. Phys. Chem. C* **2019**, *123*, 6444-6449.

8. Ravishankar, S.; Aranda, C.; Boix, P. P.; Anta, J. A.; Bisquert, J.; Garcia-Belmonte, G., Effects of Frequency Dependence of the External Quantum Efficiency of Perovskite Solar Cells. *J. Phys. Chem. Lett.* **2018**, *9*, 3099-3104.

9. Schiller, C.; Richter, F.; Gülzow, E.; Wagner, N., Relaxation Impedance as a Model for the Deactivation Mechanism of Fuel Cells Due to Carbon Monoxide Poisoning. *Phys. Chem. Chem. Phys.* **2001**, *3*, 2113-2116.

10. Kramers, H. A. La diffusion de la lumière par les atomes, Atti Cong. Intern. Fisica (Transactions of Volta Centenary Congress) Como, **1927**, *2*, 545-557.

11. Kronig, R. de L., Algemeene Theorie Der Diëlectrische En Magnetische Verliezen. *Ned. T. Natuurk* **1942**, *9*, 402.

12. Jonscher, A. K., Dielectric Relaxation in Solids. *Journal of Physics D: Applied Physics* **1999**, *32*, R57-R70.

13. Almora, O.; Zarazua, I.; Mas-Marza, E.; Mora-Sero, I.; Bisquert, J.; Garcia-

Belmonte, G., Capacitive Dark Currents, Hysteresis, and Electrode Polarization in Lead Halide Perovskite Solar Cells. *J. Phys. Chem. Lett.* **2015**, *6*, 1645-1652.

14. Kim, H.-S.; Jang, I.-H.; Ahn, N.; Choi, M.; Guerrero, A.; Bisquert, J.; Park, N.-G., Control of I-V Hysteresis in CH3NH3PbI3 Perovskite Solar Cell. *J. Phys. Chem. Lett.* **2015**, *6*, 4633–4639.

15. Yang, T.-Y.; Gregori, G.; Pellet, N.; Grätzel, M.; Maier, J., The Significance of Ion Conduction in a Hybrid Organic–Inorganic Lead-Iodide-Based Perovskite Photosensitizer. *Angew. Chem. Int. Ed.* **2015**, *54*, 7905–7910.

16. Bag, M.; Renna, L. A.; Adhikari, R. Y.; Karak, S.; Liu, F.; Lahti, P. M.; Russell, T. P.; Tuominen, M. T.; Venkataraman, D., Kinetics of Ion Transport in Perovskite Active Layers and Its Implications for Active Layer Stability. *J. Am. Chem. Soc.* **2015**, *137*, 13130-13137.

17. Sanchez, R. S.; Gonzalez-Pedro, V.; Lee, J.-W.; Park, N.-G.; Kang, Y. S.; Mora-Sero, I.; Bisquert, J., Slow Dynamic Processes in Lead Halide Perovskite Solar Cells. Characteristic Times and Hysteresis. *J. Phys. Chem. Lett.* **2014**, *5*, 2357−2363.

18. Lopez-Varo, P.; Jiménez-Tejada, J. A.; García-Rosell, M.; Ravishankar, S.; Garcia-Belmonte, G.; Bisquert, J.; Almora, O., Device Physics of Hybrid Perovskite Solar Cells: Theory and Experiment. *Adv. Energy Mater.* **2018**, *8*, 1702772.

19. Controlled Intensity Modulated Photo Spectroscopy CIMPS Manual. http://zahner.de/pdf/CIMPS.pdf. (accessed June 1, 2020)

20. Ehm, W.; Kaus, H.; Schiller, C.; Strunz, W., Z-HIT- a Simple Relation between Impedance Modulus and Phase Angle, Providing a New Way to the Validation of Electrochemical Impedance Spectra. *Proceedings of the ECS, New Trends in Electrochemical Impedance Spectroscopy (EIS) and Electrochemical Noise Analysis (ENA),* Eds. F. Mansfeld, F. Huet. OR Mattos, Electrochemical Society, Pennington, NJ **2001**, *2000*, 24.

21. Ehm, W.; Gohr, H.; Kaus, R.; Roseler, B.; Schiller, C., The Evaluation of Electrochemical Impedance Spectra Using a Modified Logarithmic Hilbert Transform. *ACH - Models Chem.* **2000**, *137*, 145-158.

22. Göhr, H.; Richter, F., Influence of soluble oxidic products from previous oxidation from platinum surfaces to the electrosorption of hydrogen, *Z. Phys. Chem.* **1979**, *115*, 69-88 (in German).

23. Meißner, W. A new method of measurement and evaluation of impedance spectra on electrodes, applied to the kinetics of anodic oxidation of silver in alkaline solution Thesis, Erlangen **1974** (in German).

24. Stoynov, Z., Impedance Modelling and Data Processing: Structural and Parametrical Estimation. *Electrochim. Acta* **1990**, *35*, 1493-1499.

25. Savova-Stoynov, B.; Stoynov, Z., Four-Dimensional Estimation of the Instantaneous Impedance. *Electrochim. Acta* **1992**, *37*, 2353-2355.

26. Kar, A., *Nanoelectronics and Materials Development*. IntechOpen: **2016**.

27. Song, T.-B.; Chen, Q.; Zhou, H.; Jiang, C.; Wang, H.-H.; Yang, Y. M.; Liu, Y.; You, J.; Yang, Y., Perovskite Solar Cells: Film Formation and Properties. *J. Mater. Chem. A* **2015**, *3*, 9032-9050.

28. Schiller, C. A.; Richter, F.; Gülzow, E.; Wagner, N., Validation and Evaluation of Electrochemical Impedance Spectra of Systems with States That Change with Time. *Phys. Chem. Chem. Phys.* **2001**, *3*, 374-378.

29. Ghahremanirad, E.; Bou, A.; Olyaee, S.; Bisquert, J., Inductive Loop in the Impedance Response of Perovskite Solar Cells Explained by Surface Polarization Model. *J. Phys. Chem. Lett.* **2017**, 1402-1406.

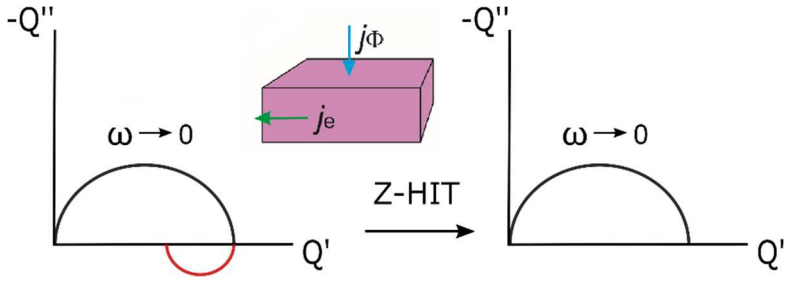

TOC graphic